

**J. F. Fohlmeister and R. F. Miller**

*J Neurophysiol* 78:1935-1947, 1997.

**You might find this additional information useful...**

---

This article cites 29 articles, 19 of which you can access free at:

<http://jn.physiology.org/cgi/content/full/78/4/1935#BIBL>

This article has been cited by 12 other HighWire hosted articles, the first 5 are:

**How the Optic Nerve Allocates Space, Energy Capacity, and Information**

J. A. Perge, K. Koch, R. Miller, P. Sterling and V. Balasubramanian

*J. Neurosci.*, June 17, 2009; 29 (24): 7917-7928.

[Abstract] [Full Text] [PDF]

**Form and Function of ON-OFF Amacrine Cells in the Amphibian Retina**

R. F. Miller, N. P. Staff and T. J. Velte

*J Neurophysiol*, May 1, 2006; 95 (5): 3171-3190.

[Abstract] [Full Text] [PDF]

**Voltage-Gated Sodium Channels Improve Contrast Sensitivity of a Retinal Ganglion Cell**

N. K. Dhingra, M. A. Freed and R. G. Smith

*J. Neurosci.*, August 31, 2005; 25 (35): 8097-8103.

[Abstract] [Full Text] [PDF]

**Encoder Adaptation Modulates the Visual Responses of Crayfish Interneurons**

R. M. Glantz and J. P. Schroeter

*J Neurophysiol*, July 1, 2004; 92 (1): 327-340.

[Abstract] [Full Text] [PDF]

**Spike Generator Limits Efficiency of Information Transfer in a Retinal Ganglion Cell**

N. K. Dhingra and R. G. Smith

*J. Neurosci.*, March 24, 2004; 24 (12): 2914-2922.

[Abstract] [Full Text] [PDF]

Medline items on this article's topics can be found at <http://highwire.stanford.edu/lists/artbytopic.dtl> on the following topics:

Physiology .. Ion Channels  
Biochemistry .. Potassium Channel  
Veterinary Science .. Ganglia  
Physiology .. Urodela  
Medicine .. Retina  
Physiology .. Tigers

Updated information and services including high-resolution figures, can be found at:

<http://jn.physiology.org/cgi/content/full/78/4/1935>

Additional material and information about *Journal of Neurophysiology* can be found at:

<http://www.the-aps.org/publications/jn>

---

This information is current as of November 30, 2009 .

# Impulse Encoding Mechanisms of Ganglion Cells in the Tiger Salamander Retina

J. F. FOHLMEISTER AND R. F. MILLER

Department of Physiology, University of Minnesota, Minneapolis, Minnesota 55455

**Fohlmeister, J. F. and R. F. Miller.** Impulse encoding mechanisms of ganglion cells in the tiger salamander retina. *J. Neurophysiol.* 78: 1935–1947, 1997. A study of nerve impulse generation in ganglion cells of the tiger salamander retina is carried out through a combination of experimental and analytic approaches, including computer simulations based on a single-compartment model. Whole cell recordings from ganglion cells were obtained using a superfused retina-eyecup preparation and studied with pharmacological and electrophysiological techniques, including phase plot analysis. Experimental efforts were guided by computer simulation studies of an excitability model consisting of five voltage- or ion-gated channels, which were identified from earlier voltage-clamp data. The ion channels include sodium, calcium, and three types of potassium channels, namely the A type ( $I_{K,A}$ ), Ca-activated potassium ( $I_{K,Ca}$ ), and the delayed rectifier ( $I_K$ ). A leakage channel was included to preserve input resistance continuity between model and experiment. Ion channel densities of Na and Ca currents ( $I_{Na}$  and  $I_{Ca}$ ) for the single-compartment model were independently determined from phase plot analysis. The  $I_K$  and  $I_{K,A}$  current densities were determined from the measured width of impulses. The  $I_{K,Ca}$  was modeled to respond to Ca influx, and a variable-rate Ca-sequestering mechanism was implemented to remove cytoplasmic calcium. Impulse frequency increases when either  $I_{Ca}$  or  $I_{K,Ca}$  is eliminated from the model or blocked pharmacologically in whole cell recording experiments. Faithful simulations of experimental data show that the ionic currents may be grouped into small ( $I_{K,Ca}$ , leakage, and stimulus), and large ( $I_{Na}$ ,  $I_K$ ,  $I_A$ ,  $I_{Ca}$ ) on the basis of their peak magnitudes throughout the impulse train. This division of the currents is reflected in their function of controlling the interspike interval (small currents) and impulse generation (large currents). Although the single-compartmental model is qualitatively successful in simulating impulse frequency behavior and its controlling mechanisms, limitations were found that specifically suggest the need to include morphological details. The spike train analysis points to a role for electrotonic currents in the control of the duration of the interspike intervals, which can be compensated by prolonged activation of  $g_{K,Ca}$  in the single-compartment model. A detailed, multicompartmental model of the ganglion cell is presented in the companion paper.

## INTRODUCTION

Voltage-clamp studies of retinal ganglion cells have identified at least five intrinsic membrane currents (Kaneda and Kaneko 1991a,b; Lasater and Witkovsky 1990; Lipton and Tauck 1987; Lukasiewicz and Werblin 1988), which appear to play a role in generating nerve impulses. These include voltage-gated  $I_{Na}$ ,  $I_{Ca}$ , the noninactivating (delayed rectifier)  $I_K$ , inactivating  $I_{K,A}$ , and  $Ca^{2+}$ -activated  $K^+$  currents  $I_{K,Ca}$ . Using these ionic currents, a model of ganglion cell impulse generation was formulated (Fohlmeister et al. 1990) in which channel-gating rate constants were established, and the magnitudes of the individual currents were adjusted to

generate impulse trains. This model yielded a large dynamic range of impulse frequencies (<1 to much greater than 100 impulses/s at 22°C) in response to constant current stimulation and appeared to provide a reasonably accurate representation of both the impulse waveform and repetitive firing behavior of ganglion cells in the tiger salamander retina.

With this model, kinetic analysis alone suggested that  $I_{K,Ca}$  might play an important role in stabilizing the cell (i.e., in preventing spontaneous firing) and in regulating the interspike interval. To better understand this mechanism, we have combined whole cell recording techniques in the intact retina-eyecup preparation with pharmacological studies and computer modeling to provide an integrated view of the experimental results, analysis, and simulation. For this purpose, nonlinear phase plot techniques have been employed to provide insight into the contribution of different ion channels to impulse shape and frequency. Our analysis suggests that  $I_{Ca}$  and  $I_{K,Ca}$  do play an important role in regulating impulse frequency. However, all channels contribute distinctive features to the impulse trains that yield significant clues to the function of neural morphology in impulse encoding. With this background, the contributions of cell geometry and nonuniform channel density distribution are subsequently explored in the companion paper (Fohlmeister and Miller 1997).

## METHODS

Ganglion cells were recorded from the tiger salamander (*Ambystoma tigrum*) retina-eyecup preparation using the whole cell recording technique (Coleman and Miller 1989; Hamil et al. 1981). The eyecup was superfused using a gravity-fed system that had a flow rate of 0.5–1.0 ml/min at a temperature of 22°C. The external Ringer solution consisted of (in mM) 111 NaCl, 2.5 KCl, 1.8  $CaCl_2$ , 1  $MgCl_2$ , 5 dextrose, and 10 *N*-2-hydroxyethylpiperazine-*N'*-2-ethanesulfonic acid (HEPES) and titrated to pH 7.80 with NaOH. Visual stimuli were provided by a computer-assisted image synthesizer (Innisfree), displayed through a monitor (Tektronix), and used at an intensity of 0.1  $\mu W/cm^2$ . Software routines gave computer control over stimulus parameters such as stimulus size, position, and intensity.

Physiological signals were recorded using a Dagan 3900 amplifier, band-pass limited to 10 kHz. The data were digitized and stored at 12-bit resolution (sampled every 200  $\mu s$ ) with an analog/digital board (Lab Master, Scientific Solutions) in a computer (Compaq 386/20) running the data acquisition package pClamp (Axon Instruments). Patch electrodes were made from 1.2 mm OD, 0.95 ID omega dot glass (Glass Co. of America) and configured on a Narashige p-88 puller, using a two-stage pulling technique. Electrodes were filled with (in mM) 98 KCl, 3.5 NaCl, 3  $MgCl_2$ , 1  $CaCl_2$ , 11 ethylene glycol-bis( $\beta$ -aminoethyl ether)-

*N,N,N',N'*-tetraacetic acid (EGTA), 5 HEPES, 2 D-glucose, 1 glutathione, 1 ATP-Mg, and 0.5 guanosine 5'-triphosphate (GTP). The pH was adjusted to 7.2 with KOH. The filled electrodes measured  $\sim 10\text{ M}\Omega$  in resistance.

A part of the results in this study required independent block of  $g_{\text{Ca}}$  and  $g_{\text{K,Ca}}$  (cf. *Calcium system*). Ca channels were blocked by adding  $250\ \mu\text{M}\ \text{Cd}^{2+}$  in the presence of normal ( $1.8\ \text{mM}$ )  $\text{Ca}^{2+}$  to the external solution or by replacing  $\text{Ca}^{2+}$  with  $1.8\ \text{mM}\ \text{Co}^{2+}$  with similar results. Ca-activated K channels were blocked by the addition of small quantities ( $10\text{--}20\ \mu\text{M}$ ) of the bee venom apamin (Hugues et al. 1982). Although  $I_{\text{K,Ca}}$  has been identified in tiger salamander (Lukasiewicz and Werblin 1988), rat (Lipton and Tauck 1987), turtle (Lasater and Witkovsky 1990), and cat (Kaneda and Kaneko 1991a), to our knowledge, it has not been evaluated for its sensitivity to apamin. Nevertheless, apamin appears to be relatively selective for the SK subclass of  $\text{Ca}^{2+}$ -activated potassium channels (Latorre et al. 1989).

It is well known that the whole cell recording mode causes eventual loss of  $I_{\text{Ca}}$  currents and, secondarily,  $I_{\text{K,Ca}}$  presumably through dilution of important cell constituents necessary to maintain these ion channels in an operational state. This time-dependent loss of  $I_{\text{Ca}}$  can be slowed by adding EGTA to the electrode solution (Chad et al. 1987) and, in neurons of *Helix aspersa*, the addition of the catalytic subunit (CS) of adenosine 3',5'-cyclicmonophosphate-dependent protein kinase and leupeptin, an inhibitor of Ca-dependent proteases. Although we added EGTA to our internal pipette solution, we did not use either CS or leupeptin in these experiments. Because the calcium current appears to be an important determinant in impulse frequency behavior of retinal ganglion cells, we carried out our experiments on the calcium system (cobalt and apamin) immediately after securing a stable whole cell recording.

Previous studies of ganglion cell function, using conventional intracellular recording techniques, correctly point out that spike amplitude is increased ( $\leq 50\%$ ) with adjustment of the capacity compensation on the amplifier (Baylor and Fettplice 1979). The attenuation of the physiological signal is due to the relatively long time constant of the high-resistance ( $> 100\ \text{M}\Omega$ ) intracellular electrode necessary for recordings from retinal cells. It should be noted that it is also possible to overadjust the capacity compensation of the amplifier, causing distortion of transient signals (Cole 1968). In contrast, the low-resistance ( $10\ \text{M}\Omega$ ) electrodes used in whole cell recording minimally distort the waveform of the action potential; adjustment of the capacity compensation increases the spike amplitude by  $\leq 5\text{--}10\%$ . In some cases, blockage of the pipette tip (presumably by cellular debris) can result in an increase of the access resistance to  $> 50\ \text{M}\Omega$ . This led to significant reductions in spike amplitude (peak voltage  $< 0\ \text{mV}$ ), which could be corrected by adjustment of the capacity compensation; however, such recordings were rejected from the present analysis.

Faithful recording of action potentials is of fundamental importance in our phase plot analysis. The use of digitized data was therefore carefully evaluated for this purpose. The phase plots consist of time derivative of membrane potential (ordinate) versus membrane potential (abscissa), except for Fig. 2C, which is current versus membrane potential. The advantage of using this version of phase plots is the ease with which one readily can identify features with the rising, peak, and falling phases of action potentials, such as the location and magnitude of the peak rate of rise or the location during the action potential cycle of features induced by calcium current, for example. To maximize this advantage, care must be taken to avoid distortions in the plots due to finite sampling; each plotted point ( $V_i$ ,  $[dV/dt]_i$ ) therefore was determined by the following formulae, which were applied to both model and physiological data

$$\text{Ordinate: } [dV/dt]_i = 5(f[i+1] - f[i]) \quad (1)$$

$$\text{Abscissa: } V_i = \frac{f[i] + f[i+1]}{2} \quad (2)$$

where  $f[i]$  is the raw (digitized) value of membrane potential at sample point  $i$  ( $1 \leq i \leq 2,047$ ). Because the actual value of  $dV/dt$  changes rapidly from one sampling point to the next during the impulses, we found the least distortion in the computed phase plots occurs by assuming the computed value of  $dV/dt$  (Eq. 1) applies to the time midway between the times of the two sampling points used in its computation. It is for this reason that the corresponding value of  $V$  is computed as the midpoint of a linear interpolation between those two sampling points (Eq. 2) as the best way of approximating the actual membrane potential at that midpoint in time. Direct use of  $V_i = f[i]$  on the other hand, introduces a marked distortion in the phase plot that increases (decreases) with increasing (decreasing) sampling interval and vanishes for the ideal of continuous sampling. Because the time rate-of-change is an approximation based on discrete sampling, the sampling interval in any case must be small in comparison with the smallest duration features (details of action potentials) that are to be resolved. Model runs with sampling intervals of 100 and 20  $\mu\text{s}$  showed no significant change or improvement over runs with 200- $\mu\text{s}$  intervals (a sampling interval of 20  $\mu\text{s}$  allows direct use of  $V_i = f[i]$  in place of the interpolation of Eq. 2 without unacceptable distortion). On the other hand, use of a 400- $\mu\text{s}$  sampling interval showed some degradation in the computed phase plots. Thus the sampling time of 200- $\mu\text{s}$  intervals was an acceptable but maximal time interval for this analysis. The factor of 5 that appears in Eq. 1 is a calibration factor to yield units of  $[\text{mV/ms}]$  (or  $\text{V/s}$ ) in place of  $[\text{mV}/0.2\ \text{ms}]$  and applies specifically to a sampling interval of 200  $\mu\text{s}$ ; in general that factor, 5, must be replaced by the number of sample points per millisecond.

### Ion channel simulation

In a single-compartment model, the five (plus leakage) ion currents, and the capacitive current may be summed according to Kirchoff's law

$$C_m \frac{dV}{dt} + \bar{g}_{\text{Na}} m^3 h (V - V_{\text{Na}}) + \bar{g}_{\text{Ca}} c^3 (V - V_{\text{Ca}}) + (\bar{g}_{\text{K}} n^4 + \bar{g}_{\text{A}} a^3 h_{\text{A}} + \bar{g}_{\text{K,Ca}}) (V - V_{\text{K}}) + \bar{g}_{\text{L}} (V - V_{\text{L}}) = I_{\text{stim}} \quad (3)$$

Of the reversal (equilibrium) potentials, only  $V_{\text{Ca}}$  was modeled as variable according to the Nernst equation, where

$$V_{\text{Ca}} = \frac{RT}{2F} \ln \{ [\text{Ca}^{2+}]_e / [\text{Ca}^{2+}]_i(t) \}, \quad (4)$$

and

$$\frac{d[\text{Ca}^{2+}]_i}{dt} = \frac{-3I_{\text{Ca}}}{2Fr} - \frac{([\text{Ca}^{2+}]_i - [\text{Ca}^{2+}]_{\text{res}})}{\tau_{\text{Ca}}} \quad (5)$$

(cf. Fohlmeister et al. 1990). The  $g_{\text{K,Ca}}$  is ligand gated according to the equation

$$g_{\text{K,Ca}} = \bar{g}_{\text{K,Ca}} \frac{([\text{Ca}^{2+}]_i / (\text{Ca}^{2+})_{\text{diss}})^2}{1 + ([\text{Ca}^{2+}]_i / (\text{Ca}^{2+})_{\text{diss}})^2} \quad (6)$$

State variables ( $m$ ,  $h$ ,  $c$ ,  $n$ ,  $a$ , and  $h_{\text{A}}$ ) of the voltage-gated channels follow the first order kinetic equations of Hodgkin-Huxely (1952)

$$dx/dt = -(\alpha_x + \beta_x)x + \alpha_x \quad (7)$$

where  $x$  is generic for the individual state variables. Rate constants and other model parameters are listed in Table 1.

### Simulated voltage-clamp data

Figure 1 presents simulated voltage-clamp data from the single-compartment model. The illustrated currents were obtained by simulated voltage-clamp steps from a holding potential of  $-65\ \text{mV}$  to

-40, -20, 0, 20, and 40 mV. Voltage-clamp data (Lipton and Tauck 1987; Lukasiewicz and Werblin 1988) were used to identify the complement of channels and to determine the presence or absence of inactivation gating. We have retained the gating stoichiometry (e.g., the exponents  $m^3$ ,  $n^4$ ) of Hodgkin and Huxley (1952), although this is an approximation and generally believed to be more complex but essentially unknown (e.g., Bezanilla and Armstrong 1977; Cole and Moore 1960). The mathematical structure of the gating kinetic rate constants is also that of Hodgkin and Huxley, which is standard in the absence of a detailed knowledge of the gating dynamics of membrane channel molecules.

### Determining gating kinetic parameters

Gating kinetic parameters were determined by a method of “trial, error, and refinement” with continuous reference to experimental spike train data. The primary templates for comparison were the shapes of the spikes (phase plots), F/I properties ( $\sim 1$  Hz/pA), and the shape of the interspike interval trajectories. For each parameter iteration, spike trains were simulated (at least) with 10 and 40 pA of stimulus current, and the stability and charging curves were determined. In the course of the  $\sim 13,500$  computer runs carried out for this study (including the companion paper Fohlmeister and Miller 1997), conductances were blocked (either individually or several), and the results compared with the corresponding experimental data runs. In the process, the wider parame-

TABLE 1. Rate constants for voltage-gated ion channels

Na <sup>+</sup> channel	$\alpha_m = \frac{-0.6(E+30)}{e^{-0.1(E+30)} - 1}$ ;	$\beta_m = 20 e^{-(E+55)/18}$
	$\alpha_h = 0.4e^{-(E+50)/20}$ ;	$\beta_h = \frac{6}{e^{-0.1(E+20)} + 1}$
Ca <sup>2+</sup> channel	$\alpha_c = \frac{-0.3(E+13)}{e^{-0.1(E+13)} - 1}$ ;	$\beta_c = 10 e^{-(E+38)/18}$
K <sup>+</sup> channel	$\alpha_n = \frac{-0.02(E+40)}{e^{-0.1(E+40)} - 1}$ ;	$\beta_n = 0.4 e^{-(E+50)/80}$
A channel	$\alpha_A = \frac{-0.006(E+90)}{e^{-0.1(E+90)} - 1}$ ;	$\beta_A = 0.1 e^{-(E+30)/10}$
	$\alpha_{h_A} = 0.04e^{-(E+70)/20}$ ;	$\beta_{h_A} = \frac{0.6}{e^{-0.1(E+40)} + 1}$

These constants operate in the first-order kinetic equation;  $dx/dt = -(\alpha_x + \beta_x)x + a_x$ . Membrane potential is in mV; temperature was modeled at 22°C.

$\bar{g}_{Na} = 50$ mS/cm <sup>2</sup>	$C_m = 1$ $\mu$ F/cm <sup>2</sup>
$\bar{g}_{Ca} = 2.2$ mS/cm <sup>2</sup>	$V_{Na} = +35$ mV
$\bar{g}_K = 12$ mS/cm <sup>2</sup>	$V_K = -75$ mV
$\bar{g}_{K,A} = 36$ mS/cm <sup>2</sup>	$V_{leakage} = -60$ to $-65$ mV
$\bar{g}_{K,Ca} = 0.05$ mS/cm <sup>2</sup>	$R_n \cong 1$ G $\Omega$

Rate constants for each of the voltage-gated ion channels simulated in this study are provided.  $I_{Na}$  and  $I_{K,A}$  both have activation ( $\alpha_m$  and  $\beta_m$  for Na activation;  $\alpha_A$  and  $\beta_A$  for the A channel) and inactivation ( $\alpha_h$  and  $\beta_h$  for Na inactivation;  $\alpha_{h_A}$  and  $\beta_{h_A}$  for A channel inactivation) kinetics. The mathematical structures of the rate constants are those of Hodgkin-Huxley (1952) throughout, and the Na- and K-channel kinetics involve only small shifts (5–10 mV) along the voltage axis relative to those of Hodgkin-Huxley. The Ca-channel activation kinetics are similar to those of the Na channel, except for a 17-mV voltage shift so that the Ca channel activates at a more depolarized level and is also slower by a factor of 2. The Ca channel has no inactivation kinetics. An important difference with the Hodgkin-Huxley model is that the 5-channel model here is considerably less conductive (by at least 1 order of magnitude) in the resting and subthreshold states. The lower portion of the table summarizes the maximum conductances for the single-compartment model used in this study. Most of these parameters remained fixed unless otherwise specified, except for  $V_{leakage}$  and  $g_{leakage}$ , which varied throughout this study.

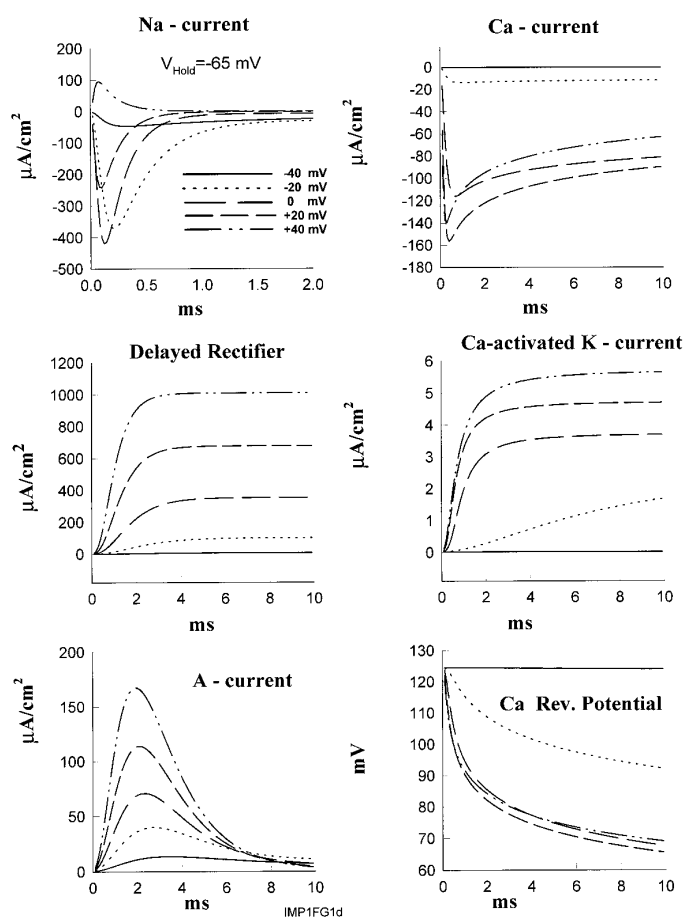


FIG. 1. Voltage-clamp records of each of the 5 ion channels modeled in this study are illustrated in addition to a simulation of the time variant change in the Ca-reversal potential in response to internal calcium concentration changes under voltage-clamp conditions. All simulations were carried out using the single-compartment model with channel kinetics and parameters summarized in Table 1. For each simulation, depolarizations were initiated from a holding potential of -65 mV and included clamp steps to -40, -20, 0, +20, and +40 mV. The time duration was 10 ms except for the Na current, which was 2 ms. Mathematical structure of the gating kinetic rate constants is that of the Hodgkin-Huxley equations (Table 1) and consisted of activation and inactivation kinetics for  $I_{Na}$  and  $I_{K,A}$ . In contrast,  $I_{Ca}$  and  $I_K$  are without inactivation kinetics. The apparent “inactivation” of the Ca current is due to increasing internal Ca concentration and the resultant change in the Ca Nernst potential (bottom right). The increasing internal Ca concentration is also responsible for the gating of the  $I_{K,Ca}$  according to Eq. 6 (middle right).

ter space was explored with the result that no secondary minima (i.e., alternative solutions) were found. A certain separation of function among the channels was discovered, permitting the determination of the rate constant parameters of the individual channels.

Thus the structure of the rate constants in essence contain two parameters each (Table 1). One of these is an overall constant (e.g., 0.6 in the case of  $\alpha_m$ ) that fixes the time rate of gating; the other (e.g., 30 mV in  $\alpha_m$ ) locates the channel gating range along the voltage axis. For example, comparing the activation rate constants ( $\alpha$  and  $\beta$ ) of the Na and Ca channels will show that the Na channel is twice as fast as the Ca channel (0.6 vs. 0.3 in  $\alpha$ , and 20 vs. 10 in  $\beta$ ) and that an equivalent level of activation requires 17 mV of additional depolarization for the Ca channel as compared with the Na channel (parameter values 13 vs. 30 mV in  $\alpha$ , and 38 vs. 55 mV in  $\beta$ ). This 17-mV shift was determined from a comparison of experimental impulse responses with Ca and then Na chan-

nels blocked individually. Similar considerations were applied to the K and A channels for the falling phase of action potentials. The model voltage-clamp records for  $I_{Na}$  and  $I_K$  in Fig. 1 resemble (but are not equal to) those of the Hodgkin-Huxley (1952) model. The activation component of  $I_{K,A}$  is somewhat similar to that of the delayed rectifier; it is distinguished from the delayed rectifier by the presence of an inactivation mechanism (Conner and Stevens 1971). Given the experimental variability in responses and the standard mathematical structure for gating kinetics, we found that all spiking parameters could be determined to within  $\sim 20\%$  without introducing unacceptable distortions.

With the parameters of these large spiking currents uniquely adjusted according to the phase plots and in the absence of  $\bar{g}_{K,Ca}$ , the model cell exhibits both instability (i.e., spontaneous firing), and a flat F/I curve with relatively high impulse frequencies for all levels of stimulus current. This agreed with experiment when apamin was applied. The calcium-activated K current then restored both stability and the virtually proportional F/I curves seen experimentally. The magnitude of  $I_{K,Ca}$  is set in the process. As a welcome byproduct, this current also reproduced the experimental interspike trajectories.

The standard membrane capacitance,  $C_m = 1 \mu\text{F}/\text{cm}^2$ , which yields capacitive current of  $I_c = C_m dV/dt$ , sets the *absolute* magnitude scale for the ionic currents in Eq. 3 (i.e., determines the values of  $\bar{g}_x$ ). Specifically, the magnitudes of  $\bar{g}_{Na}$ ,  $\bar{g}_K$ , and  $\bar{g}_{K,A}$  are determined from a comparison of the peak rates of rise and fall between experimental and model generated impulses in phase plots in the presence of the well-established value of membrane capacitance. The calcium current provides a unique signature during the latter part of the falling phase of action potentials and can be determined accurately in phase plots.

Because the kinetics of the  $I_{Ca}$  are about a factor of 2 slower and the voltage dependence of the rate constants is shifted by  $\sim 17$  mV in the depolarized direction relative to the  $I_{Na}$  kinetics,  $I_{Ca}$  turns on somewhat later than  $I_{Na}$ , and, under current-clamp conditions, it appears only after  $\text{Na}^+$  activation has initiated the action potential. Thus the Ca current, when present, has negligible effect on the peak rate of rise of an action potential and begins to manifest itself only as the impulse peak is approached. One report (Karschin and Lipton 1989) found low-threshold (T-type) calcium channels in some ganglion cells of the neonatal rat retina, and we have seen evidence of this current in dissociated ganglion cells of the tiger salamander retina. However, this current is small and has not been included in the present study. To date, T-type calcium channels have not been described in adult cells of cat or turtle (Kaneda and Kaneko 1991a; Lasater and Witkovsky 1990; Lukasiewicz and Werblin 1988). Our model of calcium channels thus is confined to a high-threshold (L-type) mechanism.

Unlike the  $\text{Na}^+$  channel, the  $\text{Ca}^{2+}$  channel has no inactivation kinetics. The reduction in  $\text{Ca}^{2+}$  current after an initial peak value in the voltage-clamp records (Fig. 1) is due to the concentration-dependent (therefore time-dependent) properties of the  $\text{Ca}^{2+}$  reversal potential (Kaneda and Kaneko 1991a). The  $\text{Ca}^{2+}$  current was modeled with a time-dependent reversal potential,  $V_{Ca}$ , because the low residual intracellular  $\text{Ca}^{2+}$  concentration ( $10^{-7}$  M) can be increased substantially by  $\text{Ca}^{2+}$  influx during activation (Fig. 1, *bottom right*). It is this change in concentration that is solely responsible for the regulation of the Ca-activated K-current,  $I_{K,Ca}$  (Eq. 6). Thus  $I_{K,Ca}$  has an apparent voltage dependence, but no independent voltage-gating was modeled for this current. Therefore the  $I_{K,Ca}$  is a model of the SK subtypes (Hugues et al. 1982), which are apamin sensitive. The calcium dissociation constant is  $[\text{Ca}]_{\text{diss}} = 10^{-6}$  M; at this level,  $g_{K,Ca}$  is half-activated. The magnitude of  $\bar{g}_{K,Ca}$  is determined from cell stability and the F/I properties of the experimental impulse trains. We find that these parameters are determined more reliably and accurately by spike train analysis than from voltage-clamp data, which often is distorted by an inadequate

space clamp. Cell stability and charging parameters were determined in a single run of 2,400-ms duration; the model neuron was allowed to settle to its resting state (stability) for the initial 1,200 ms of the run (i.e., until steady state), at which time, a hyperpolarizing current was applied and the input resistance and time constant (charging parameters) were determined. We assumed a single spherical compartment [specifically for purposes of computing  $[\text{Ca}]_i(t)$ ] of  $25 \mu\text{m}$  diam (for similarity to ganglion cell somas), and uniform channel densities,  $\bar{g}_x$ , as listed in Table 1. In response to hyperpolarizing current steps, this model yielded an input resistance ( $R_N$ ) of several tens of gigaohms in the absence of a leakage conductance. To preserve homology with the physiological observations, a leakage conductance was added ( $g_L = 0.05 \text{ mS}/\text{cm}^2$ ), thus yielding an input resistance of  $\sim 1 \text{ G}\Omega$ .

### Action potentials

Figure 2A gives a model action potential from an impulse train evoked with  $0.5 \mu\text{A}/\text{cm}^2$  ( $= 10 \text{ pA}$ ) stimulus current. Note the smooth waveform with no obvious shoulders or "notches" in either the rising or falling phases. On the same time base, Fig. 2B gives the course of the five individual ionic currents, and their algebraic sum,  $\Sigma I_{\text{ion}}$  (heavy curve). Noteworthy features are that  $I_{Ca}$  activates with some delay relative to  $I_{Na}$  and, particularly, that  $I_{K,Ca}$  remains negligible in comparison with these currents. This last feature allows the complement of currents to be grouped into two classes on the basis of their relative magnitudes achieved during an impulse train; thus  $I_{Na}$ ,  $I_K$ ,  $I_{K,A}$ , and  $I_{Ca}$  become large and are responsible for generating and shaping the impulses, whereas  $I_{K,Ca}$ , leakage, and stimulus currents remain small throughout, but play important roles in determining the duration of interspike intervals (i.e., the impulse frequency, see Fig. 3, below).

The action potentials recorded with low-resistance patch electrodes have peak amplitudes that typically range from 70 to 90 mV (level of interspike trajectory to peak). However, because of tonic synaptic activity, different types of retinal ganglion cells (RGCs) can have different dark "resting" (i.e., steady state) potentials that range from  $-70$  to  $-45$  mV (Belgum et al. 1983; Coleman and Miller 1989; Frumkes et al. 1981). For the purposes of this study, we established a general rule that the impulses should have an overshoot of  $+10$  to  $+20$  mV to be considered acceptable.

### Phase plot of ionic currents

Figure 2C gives plots of the individual ionic currents versus membrane potential during the impulse illustrated in Fig. 2, A and B. A constructive approach to this plot is to begin with the trajectory that represents the sum of the ionic currents,  $\Sigma I_{\text{ion}}$  (heavy curve), which advances counterclockwise around the loop; time markers are provided at 0.05-ms intervals. In this single-compartment (space-clamped) model, the sum of the ionic currents  $\Sigma I_{\text{ion}}$  is equal and opposite to the capacitive current,  $C_m dV/dt$ , except for the negligible stimulus current offset of  $0.5 \mu\text{A}/\text{cm}^2$  (Fig. 3). Because much of the analysis will use phase plots of  $dV/dt$  versus  $V$ , we note the near equivalence of  $\Sigma I_{\text{ion}}$  and  $dV/dt$ , except for a minus sign, which causes a mirror symmetric reflection about the zero current axis (compare Figs. 2C, 4, and 5); the overall constant scale factor,  $C_m$ , happens to be equal to unity (1) when the units are microamperes per square centimeter and microfarads per square centimeter as is the case here. The equivalence of  $\Sigma I_{\text{ion}}$  and  $-dV/dt$  was used to determine the values of the channel conductances,  $\bar{g}_x$ , in Table 1 by a quantitative comparison of experimental and model phase plots (Figs. 4 and 5). Note also in Fig. 2C the very small amount of current carried by  $I_{K,Ca}$  denoted by  $K_{Ca}$ .

### Interspike interval

Due to a scaling problem, the contribution of the Ca-activated K current is difficult to appreciate in the plots of Fig. 2. For this

Single Compartment Model

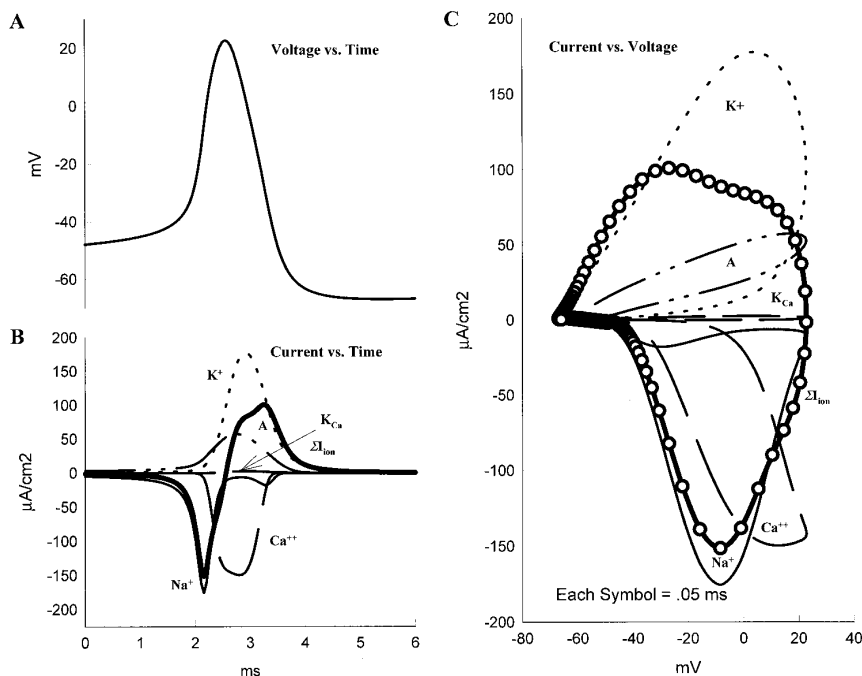


FIG. 2. A summary of simulated impulse behavior based on a single-compartment model. *A*: waveform of a single impulse during a train of action potentials. *B*: on the same time base, 5 individual ionic currents modeled in this study, including  $I_{Na}$ ,  $I_K$ ,  $I_{K,A}$ ,  $I_{Ca}$ , and  $I_{K,Ca}$  ( $K_{Ca}$ ), and the resulting net transmembrane ionic current (dark line  $\Sigma I_{ion}$ ). *C*: phase plots of current vs. membrane potential during the impulse and illustrations of the 5 different ionic subcomponents which contribute to the total transmembrane ionic current (dark line  $\Sigma I_{ion}$ ). Inwardly directed current is downward (negative) by convention, and the  $\Sigma I_{ion}$  trajectory advances in a counterclockwise direction with time markers at 0.05-ms intervals. Rapid rising phase of the impulse is entirely due to  $I_{Na}$ , whereas the  $Ca^{2+}$  current is delayed in onset. During the repolarization phase (*top* of phase plot), both the  $I_A$  (*A*) and the delayed rectifier ( $K^+$ ) contribute substantially. Note that  $I_{K,Ca}$  ( $K_{Ca}$ ) provides only a negligible current to the action potential.

reason, we constructed Fig. 3 to illustrate a model impulse train (*top*) generated with 20 pA ( $1 \mu A/cm^2$ ) of stimulus current. Figure 3, *bottom*, shows current records appropriately scaled to resolve the individual currents during the interspike intervals. The currents therefore are clipped as the records approach each active impulse phase. The major currents ( $I_{Na}$ ,  $I_K$ , and  $I_{K,A}$ ) increase monotonically with increasing rate throughout the interspike intervals.  $I_{K,Ca}$  becomes prominent and dominates most of the interspike trajectory after the first action potential loads the cell with ionic calcium. Figure 3 therefore demonstrates the significance of  $g_{K,Ca}$  in the

interspike interval and its control of impulse frequency in a single-compartment model. Some of this function of  $I_{K,Ca}$  (i.e., control of  $F/I$ ) is shared by longitudinal (electrotonic) currents, which are comparable in magnitude in a multicompartment model; however,  $I_{K,Ca}$  retains its important function of stabilizing the cell there. Note that the model  $I_{Ca}$  is virtually zero throughout the interspike interval and activates abruptly during the early rising phase of each impulse. Comparing  $I_{Na}$  with  $I_{Ca}$  in this figure may appear to imply that the activation kinetics of  $I_{Ca}$  are faster than those of  $I_{Na}$ . The converse is actually the case, and the increasing Na activation seen here is in response to the slow depolarization during the interspike interval, at which level Ca activation gating is negligible (cf. Fig. 2 and Table 1).

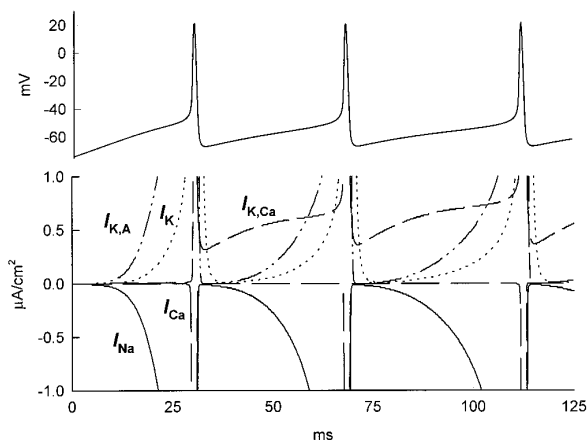


FIG. 3. *Top*: illustration of repetitive impulse activity generated by 20 pA injected into a single-compartment cell. *Bottom*: on the same time base, individual ionic currents are illustrated on a scale that allows the currents to be well resolved during the interspike intervals; large currents associated with the impulses therefore are clipped (see Fig. 2). As the trajectories approach the impulses, the  $I_{Na}$ ,  $I_A$  (*A*), and  $I_K$  ( $K^+$ ) are strongly activated, whereas  $I_{Ca}$  is delayed in onset. Calcium loading of the cell strongly activates the  $I_{K,Ca}$  ( $K_{Ca}$ ), but only after the first impulse has occurred. Note that  $I_{K,Ca}$  is the dominant current during the early portion of the interspike interval and subsequently gives way to  $I_{Na}$  and the other  $K^+$  currents. Thus this magnified view suggests that  $I_{K,Ca}$  plays an important role in regulating the time interval between impulses.

RESULTS

Impulse frequency response ( $F/I$ )

MODEL BEHAVIOR. Figure 4 (*left*) illustrates the model generated impulse trains in response to depolarizing currents, which range from 0.5 to  $2.5 \mu A/cm^2$  ( $\sim 10$ – $50$  pA in the spherical soma). Figure 4, *right*, illustrates the corresponding phase plots,  $dV/dt$  versus  $V$  (*Eqs. 1* and *2*). The phase plots are superposed for comparison among the five spike train records (plots are distinguished by different symbols) and cover the full length of each record. The trajectories advance clockwise around the loop; the peaks of the action potentials occur at the extreme right of the plot, where  $dV/dt = 0$ , and the peak rate of rise occurs at the top where  $dV/dt$  is maximum. The plots for the separate traces are quite similar, indicating that the overall impulse waveform is conserved across frequencies (or levels of stimulus).

PHYSIOLOGICAL BEHAVIOR. Figure 5 (*left*) illustrates the impulse trains generated by an OFF retinal ganglion cell studied under whole cell recording conditions and illustrates the increase in impulse frequency in response to increasing currents (10–50 pA) applied through the patch microelectrode.

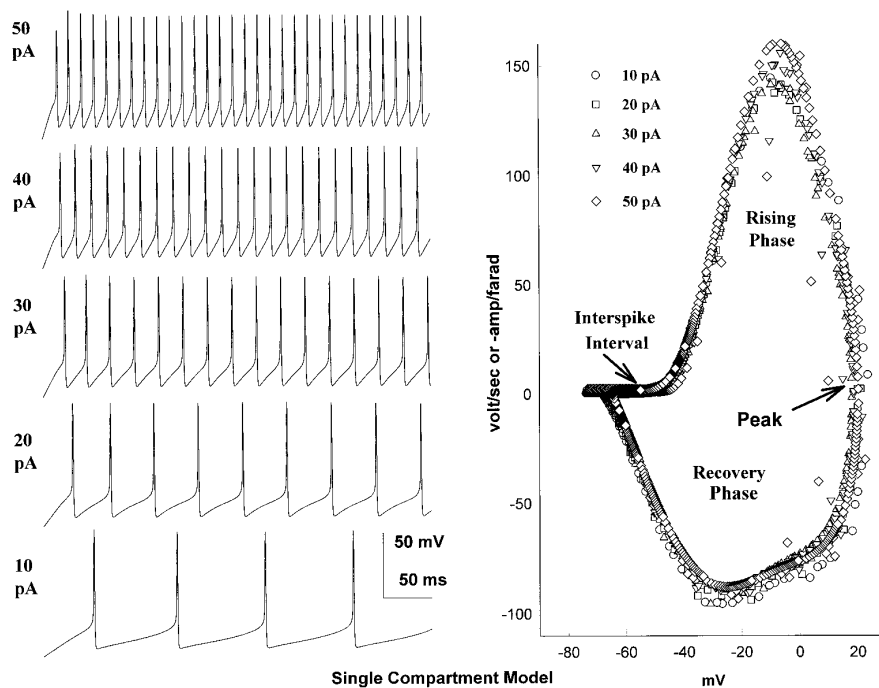


FIG. 4. Impulse trains were generated in a single-compartment model (Table 1), with 5 voltage-sensitive ion channels (+ leakage) in response to depolarizing step currents of 10–50 pA. Note the graded increase in impulse frequency over the range of currents used. *Right*: phase plots shown of  $dV/dt$  vs.  $V$  of the 5 impulse trains (*left*) in which the trajectories move clockwise around the loop. In this plot,  $dV/dt$  (volts/s) can be interchanged with  $-\Sigma I_{ion}$  (–amp/farad) because the membrane capacitance is unity ( $1 \mu\text{F}/\text{cm}^2$ ) and stimulus current is negligible. Thus the mirror symmetry between this phase plot and the phase plot in Fig. 2. Rising phase of the impulse is upward, and a different symbol was used to distinguish the impulse trains. Trajectories consist of a fast rising phase and peak response followed by a more gradual recovery phase (*bottom*). Interspike intervals are revealed as the relatively flat portion on the *left* side of the plot.

When 10 pA of current was applied, a long initial trajectory (or latency) was observed before the first impulse. Firing frequency increased, and the initial latency decreased, with increasing levels of step current. The initial latency was observed in every recorded cell. Its duration was generally comparable with the duration of the subsequent interspike intervals in steady state. It was therefore most dramatic with the lower stimuli (10 pA) because these also generate the lowest impulse frequencies. Among the cells the variations of the initial latency ranged from 20% shorter to 50% longer than the subsequent interspike intervals in steady state. Some adaptation or accommodation also was observed, although this was highly variable and occurred mainly with the larger stimulus currents (higher frequencies). Figure 5, *right*, shows the phase plots for each of the traces on the *left* using a different symbol for each record. Like the model, the phase plots show remarkable similarity in the rate of rise, the maximum amplitude, and the rate of recovery during the falling phase across the set of records.

Although there is general agreement between model and physiological records, some systematic differences do exist: 1) the single-compartment model does not exhibit the long latency to first spike; 2) the model impulse frequency rises more steeply with increasing stimulus current, leading to some disagreement in the impulse frequency versus stimulus current ( $F/I$ ) curve for 40 and 50 pA; and 3) the shapes of the falling phases of impulses disagree in the phase plots. All three of these features are a direct result of the constraints imposed by use of a single-compartment configuration. The first two discrepancies cannot be eliminated within the parameter space provided by the five-channel model considered here (cf. *Determining gating kinetic parameters*). These two discrepancies deal with phenomena in the sub-threshold (interspike intervals) region and are constrained here by the fixed membrane area of the single-compartment configuration, which prevents the possibility of electrotonic

dispersal of the stimulus current into dendrites and axon. This effect is observed clearly in the multicompartment simulations, in which the first two discrepancies vanish automatically. The last item, namely the increased rate of fall during the latter half of the falling phase of impulses as seen in the model phase plots, could be corrected by reducing the calcium current. A consequence of such reduction, however, is reduced activation of  $I_{K,Ca}$ , and the attendant loss of low-frequency repetitive firing in a single-compartment model.

#### Physiological action of apamin

Modeling analysis predicts that elimination of the  $I_{K,Ca}$  current should increase the frequency of repetitive firing in ganglion cells. To test this possibility, we carried out experiments in which apamin was added to the bathing medium to selectively block this current. It is essential in these experiments to ensure that apamin does not change the input resistance of the cell. Input resistance therefore was monitored by intermittent application of hyperpolarizing current pulses ( $\leq 5$  pA). We found that apamin did not change the input resistance of any cell tested. Figure 6A shows a control, whole cell recording from an RGC in response to 10 pA of current injection; Fig. 6B gives the result after apamin was applied and illustrates the increase in frequency of firing. If the action of apamin is solely to block the  $I_{K,Ca}$ , then phase plots of the impulse activity should show very little difference in waveform with and without apamin because  $I_{K,Ca}$  contributes virtually nothing to the impulse itself. The closed and open circles of the phase plots presented in Fig. 6C confirm that the impulse has been imperceptibly altered by apamin. Figure 6, D–F, illustrates the same general result with  $I_{K,Ca}$  eliminated from the single-compartment model.

#### Physiological action of blocking the calcium current

Figure 7 (*top*) illustrates a physiological, whole cell recording from an RGC under control conditions (—) super-

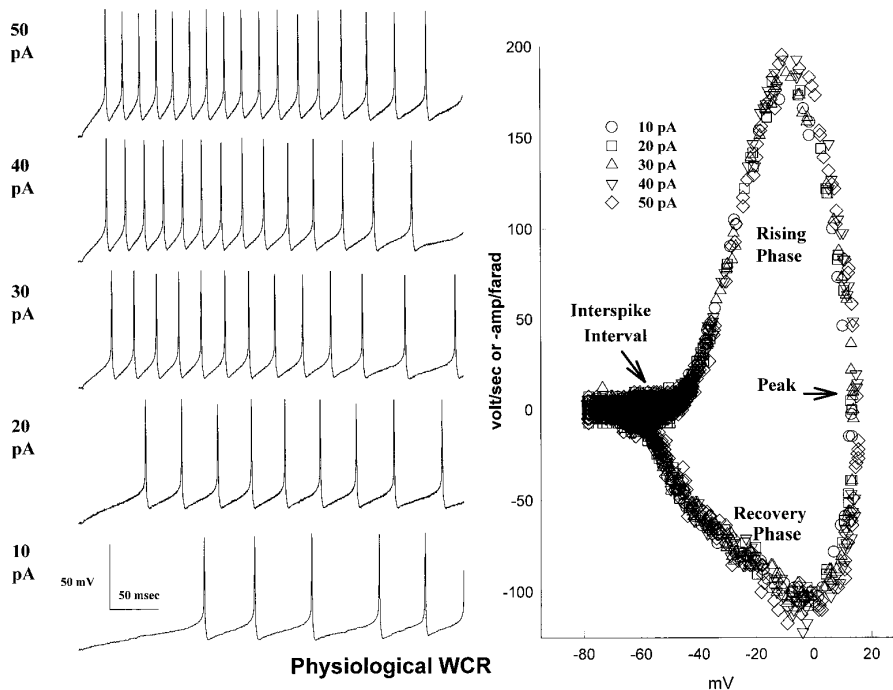


FIG. 5. Whole cell recordings from an OFF ganglion cell in response to depolarizing current injections of 10–50 pA. An orderly progression of increasing impulse frequency in response to the increasing levels of current injection appears qualitatively similar to the modeling results presented previously (Fig. 4). A decline in impulse frequency (adaptation) can be seen during the latter portions of most of these impulse trains. Phase plots corresponding to those of Fig. 4 are given (right) using a different symbol for each record on the left.

imposed on a recording from the same cell after cobalt was substituted to eliminate the calcium current (dashed line). Although cobalt substitution often increases the input resistance of ganglion cells, presumably because it reduces or shuts down otherwise tonically activated synaptic inputs, we were able to observe a number of ganglion cells in which cobalt application did not change  $R_N$ . Note that the initial charging response to the current pulse is the same for both traces, an indication that cobalt substitution did not significantly change the input resistance or time constant of the cell. Nevertheless, it is clear that cobalt substitution did increase the frequency of firing, and simultaneously also reduced the amplitude of the nerve impulses. The increased firing frequency is associated with an obvious shift of the interspike voltage trajectory in the depolarizing direction, with a simultaneous reduction in the impulse overshoot. Figure 7, *bottom*, gives the results obtained when the calcium current was eliminated from the single-compartment model; the impulse frequency is increased and the impulse overshoot is reduced, indicating reasonable fidelity with the physiological observation. Comparison of the physiological and modeling results supports the conclusion that the calcium current participates in controlling the impulse frequency in RGCs of the tiger salamander retina.

#### Calcium system (model)

In a series of simulations, the calcium conductance,  $\bar{g}_{Ca}$ , was varied in steps from 0 to 8.0 mS/cm<sup>2</sup>, and a train of action potentials was generated as given in Fig. 8. Note that the frequency of impulses decreases as the calcium conductance increases. The phase plots on the *right* illustrate the dramatic differences effected by calcium current in the shape of impulses.  $I_{Ca}$  gives a primary signature at two locations in phase plots: it expresses itself at the peak of the action potential (*rightmost* region of the phase plot) and during the

latter half of the falling phase of the action potential. Thus the Na current initiates the spike, the early regenerative depolarization of which then activates the Ca channels. Under our “standard” conditions for the single-compartment model (Table 1;  $\bar{g}_{Ca} = 2.2$  mS/cm<sup>2</sup>), the Ca current adds some 5–10 mV to the impulse peak because of its large, positive reversal potential, even though the magnitude of the calcium conductance is comparatively small.

The influence of the Ca current on the latter half of the falling phase of spikes is more complex but highly diagnostic. The absence of calcium current always leads to a relative slowing in the rate of change of membrane potential during the latter portion of the recovery phase (a “deflating” of the phase plot trajectory). As Ca current is increased, that portion of the phase plot increasingly bulges downward, indicating increasing (negative) time rate of change. Larger values of  $\bar{g}_{Ca}$  add a notch to the phase space trajectory during the falling phase (Fig. 8,  $\bar{g}_{Ca} = 8$ ). Additional large K currents could obscure the notch, but not the Ca-diagnostic degree of downward bulging in the latter half of the falling phase; simulations have shown that K currents manifest themselves strongly during the earlier portion of the falling phase because the K-ionic driving force,  $V - V_K$ , is then large. Therefore, although there is a degree of overlap in the downward bulging effect generated by the two currents (Ca and K), there is sufficient separation to definitively conclude that the model value of  $\bar{g}_{Ca} = 2.2$  mS/cm<sup>2</sup> is too large to properly match the physiological observations (compare Figs. 4 and 5) and that the model action potential falls off more steeply in its latter portion than seen experimentally. The notch in Fig. 8 is the primary cause of the notch in Fig. 8 is the tendency of the Ca current to create “plateau” action potentials (which are ultimately characteristic of cardiac Purkinje cells, which involve large Ca currents). The notch in Fig. 8 implies that the rate of recovery slows toward a plateau before descending more steeply again, although a

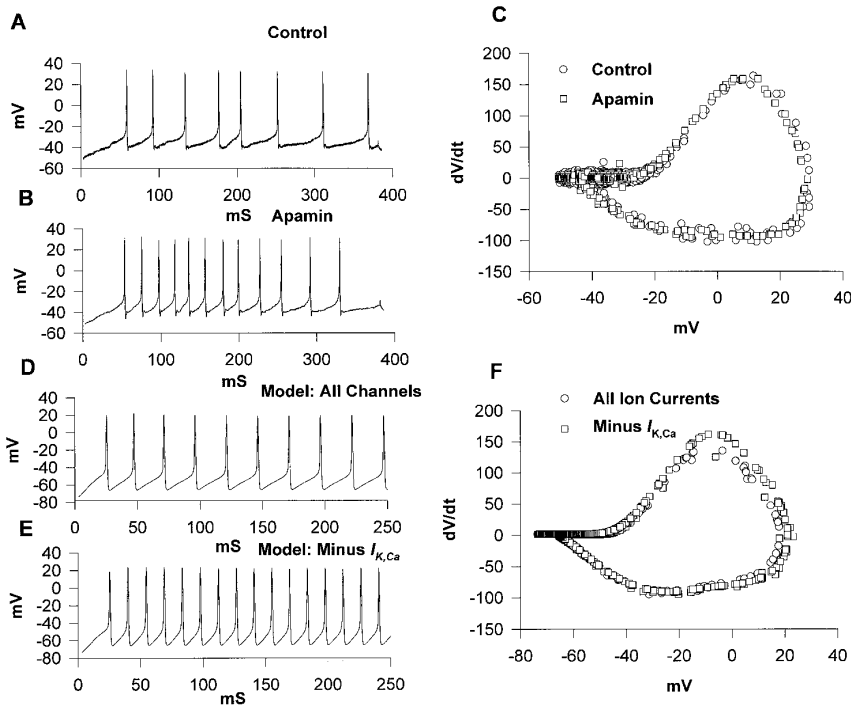


FIG. 6. Comparison of the effects of apamin application in physiological whole cell recording (A–C) and removal (or blockage) of the  $I_{K,Ca}$  in the single compartment model (D–F). Bee venom apamin is thought to selectively block  $I_{K,Ca}$ . Impulse frequency increases with apamin application (B) or removal of  $I_{K,Ca}$  (E) relative to controls (A and D), with small and only negligible changes in the impulses themselves as indicated in the phase plots (C and F), in which test and control records are superimposed.  $R_N$  remained unchanged with apamin application, and the small differences between the model control and test phase plots reflect effects of the single-compartment approximation. General agreement between control and test phase plots shows that  $I_{K,Ca}$  contributes little to the impulse waveform.

plateau is not actually formed. (Technically, a plateau would require  $dV/dt$  to reach zero during the falling phase of the phase plot trajectory.)

#### Calcium-activated potassium current and cell morphology

The Ca-activated K-current ( $I_{K,Ca}$ ) is intimately associated with the Ca current because intracellular free Ca provides the gating of  $I_{K,Ca}$ . The  $I_{K,Ca}$  gives virtually no signature in phase plots because of its small size during impulses. As

noted above, however,  $I_{K,Ca}$  is comparable in magnitude with physiological levels of stimulus current and, for this reason, has a strong influence on the regulation of impulse frequency and the F/I properties of the cell. Because extended cell morphology also exerts an influence on the control of impulse frequency, the parameters of the Ca system (specifically  $\bar{g}_{Ca}$ ,  $\bar{g}_{K,Ca}$ , and  $\tau_{Ca}$ ) are distorted in our single-compartment model so as to partially compensate for the absence of geometric effects (Fohlmeister and Miller 1997). The objective of these alterations was to formulate a single-com-

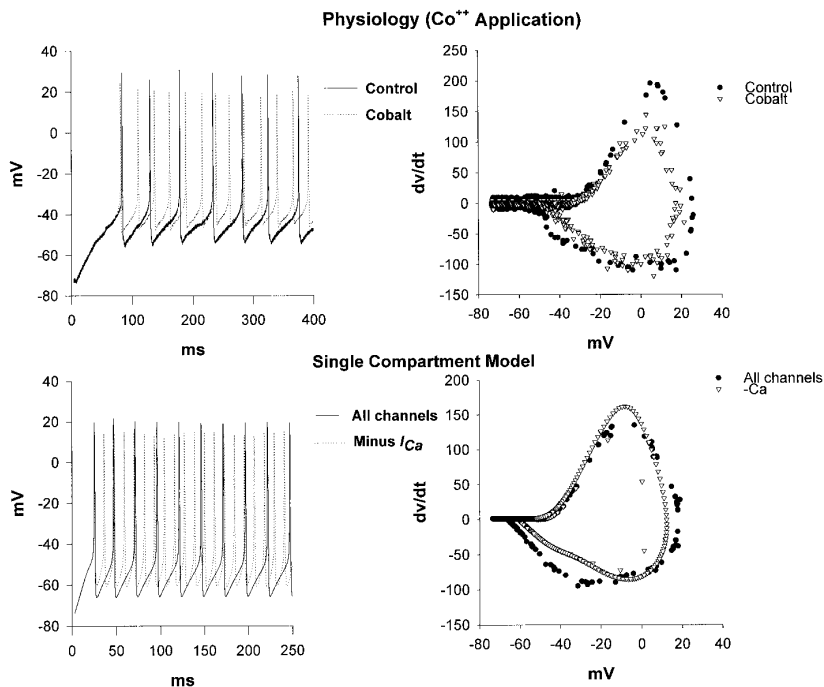


FIG. 7. Comparison of the effects of Ca-channel blockage on physiology and the single compartment model. Ca current was blocked by cobalt substitution for calcium. *Top*: control record shown (—) and a test record (---). It was important in this comparison that Co substitution did not cause an increase in input resistance. Note that the initial charging traces leading to the first impulses in both control and test records are identical, indicating no change in  $R_N$ . Both model (*bottom*) and physiology test records show a similar increase in impulse frequency relative to their controls and furthermore show similar effects on the spike amplitudes and undershoots.

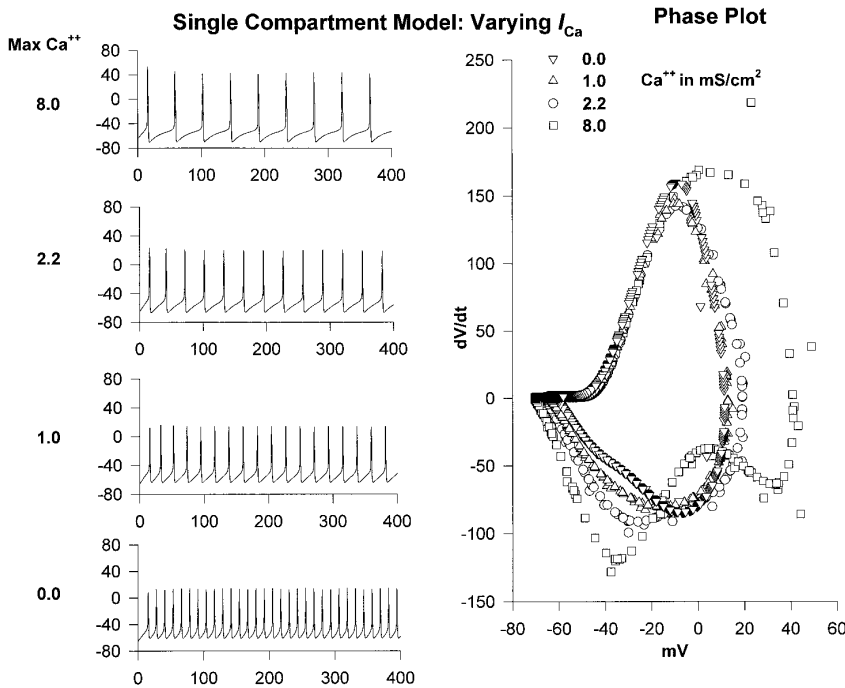


FIG. 8. Effect of changing the Ca current on impulse waveform and frequency. Impulse trains were generated by the single-compartment model in response to 20 pA of stimulus current with  $\bar{g}_{Ca}$  in the range of 0–8 mS/cm<sup>2</sup> (left). Note the increase in frequency with declining Ca current (cf. Fig. 7). Phase plots of these records are given (right). Phase plot of  $\bar{g}_{Ca} = 1.0$  mS/cm<sup>2</sup> corrects the trajectory in the latter portion of the falling phase (–20 to –60 mV) relative to that given for  $\bar{g}_{Ca} = 2.2$  mS/cm<sup>2</sup>. Phase plot of  $\bar{g}_{Ca} = 8.0$  mS/cm<sup>2</sup> shows a pronounced notch during the falling phase. This notch reflects a decline in the rate of repolarization and implies a tendency toward generating plateau action potentials. The apparent “noise” in these model phase plots is due to the different shapes of the initial (“transient”) impulses before each record settles into steady state spiking.

partment model that reproduced the experimental F/I properties as closely as possible under normal physiological conditions. The high level of  $\bar{g}_{Ca}$  used here causes increased activation of  $I_{K,Ca}$ , and the long Ca removal time  $\tau_{Ca}$  (50 ms) maintains the increased activation to produce longer interspike intervals. Cell morphology takes over some of the function of increasing the interspike interval durations, a phenomenon also related to the increased latency to first spike seen under low-stimulus conditions.

*Current magnitudes and the nerve impulse*

Figure 9 was constructed to better appreciate the role of  $I_{K,Ca}$  under modeling conditions and to demonstrate the effect of current magnitudes on the impulse waveform as reflected in the phase plot. Figure 9, top, presents model impulses under conditions in which the ion channel conductances are halved systematically relative to the control trace (1). Corresponding phase plots are given in Fig. 9, bottom. When all currents are reduced by 50% (condition 2), a reduction in impulse amplitude, as well as a lengthening of the interspike interval (indicated by the relative positions of the impulses) is observed. The causes of these effects are that reduced  $I_{Na}$  increases the time required to reach threshold, and the reduced spike amplitude (controlled by both  $I_{Na}$  and  $I_{Ca}$ ) leads to lower activation of both  $I_K$  and  $I_{K,Ca}$ . When  $I_{K,Ca}$  alone is restored to its full value (condition 3), the interspike interval is further lengthened, as expected, but there is virtually no change in the impulse itself as indicated in the phase plots (conditions 2 and 3). When, in addition,  $I_{Ca}$  is restored to its full value (condition 4), three significant effects may be observed in the phase plots: the impulse peak is restored almost to the control value, but  $I_{Ca}$  has virtually no effect on the rate of rise of the action potential, which is controlled solely by  $I_{Na}$ . Finally, the Ca signature in the falling phase of action potentials is restored, even though the falling rate

of change,  $-dV/dt$ , remains less than control because of the reduced  $I_K$  and  $I_{K,Ca}$ .

*Leakage conductance and charging curve*

Thus far the spike train analysis has made no reference to a leakage current. Much of the modeling in this analysis was done in the absence of leakage, because leakage plays a very minor role in shaping the impulse waveform and determining the range of frequencies evoked by depolarizing step currents into single-compartment models. However, a hyperpolarizing current step used to evaluate the passive properties of the model reveals an input resistance of many tens of seconds of gigaohms in the absence of leakage, in contrast to the experimental value of  $\sim 1$  G $\Omega$  (Table 2). More importantly, the time constant of the model cell in the absence of leakage is hundreds of milliseconds, whereas that of the physiological cell is in the range of 40–120 ms. This discrepancy is remedied by the inclusion of a leakage conductance of  $g_L = 0.05$  mS/cm<sup>2</sup> to the model cell. Inclusion of  $g_L$  is responsible for providing a nearly exponential charging curve with a time constant of about  $\tau = 50$  ms. Both the nearly exponential shape and the value of the time constant fall within the range of physiological observation.

Figure 10 gives model records in response to 1  $\mu$ A/cm<sup>2</sup> ( $\sim 20$  pA into the spherical soma) of injected current, both in the absence (solid line) and presence of 0.05 mS/cm<sup>2</sup> of leakage conductance (dashed line). The leakage reversal potential was  $-62$  mV, and similar records may be generated for any value in the range of  $-65 < V_L < -60$  mV. Although in this example of relatively low-stimulus current the impulse frequency decreased, the addition of a leakage conductance is of little help in correcting the overall steepness of the F/I curve associated with the single-compartment approximation. Apart from cor-

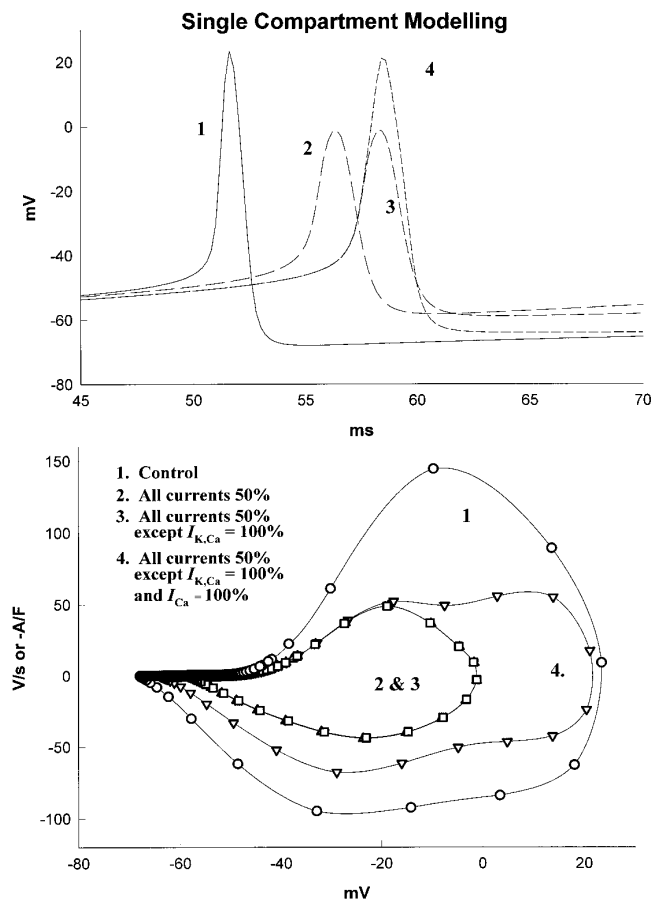


FIG. 9. These examples were taken from a single-compartment model in which the ionic currents of this study were altered to better appreciate their impact on impulse waveform and frequency. *Trace 1*: normal impulse during a train in a single compartmental model. *Trace 2*: a small and somewhat delayed impulse, indicating a somewhat longer interspike interval when all currents are reduced by 50%. *Trace 3*: produced by keeping all currents at the 50% level, except the  $I_{K,Ca}$ , which was returned to 100%. In this case, the amplitude and waveform of the impulse is virtually identical to that in *Trace 2*, but the impulse is further delayed because  $I_{K,Ca}$  provides additional hyperpolarization and delay to the onset of the impulse. In *Trace 4*, both  $I_{K,Ca}$  and  $I_{Ca}$  were returned to 100% with the other currents remaining at 50%. In this case, the rising phase of the impulse is virtually superimposed on *Trace 3*, but the amplitude is now much larger, because  $I_{Ca}$  contributes to the amplitude of the impulse. Note also the increased width due to the reduced K currents. *Bottom*: phase plots provide impulse waveform information on the 4 simulations presented above. *Trace 2* is a smaller version of *Trace 1* with an otherwise similar phase plot trajectory. *Trace 3* can be superimposed on *trace 2* because, even though  $I_{K,Ca}$  has been restored to 100%, it has virtually no effect on the impulse waveform: its principle action is on the interspike interval. *Trace 4* shows a bilobed trajectory, with a decrease in rate of voltage rise (due to the low Na current) as the slower calcium current comes into play but with a close to normal impulse peak amplitude. The repolarization shows a second hump, a signature of substantial calcium current.

recting the charging curve in response to hyperpolarizing currents, we note that leakage has little effect on the shape of the interspike trajectory or the impulse waveform as indicated by the phase plots in Fig. 10. Despite its relatively large size as compared with  $g_{K,Ca}$ , the leakage conductance is relatively innocuous in its effect on the shape of the interspike potential trajectory because that trajectory straddles the leakage reversal potential.

TABLE 2. *Physiological ganglion cell groups derived from impulse entrainment*

	Fast	Medium	Slow
$R_n$ , $G\Omega$	$1.45 \pm 0.43$	$0.86 \pm 0.31^*$	$1.02 \pm 0.54^\dagger$
Max	2.2	1.2	1.8
Min	0.6	0.5	0.4
$\tau_0$ , ms	$65 \pm 19$	$46 \pm 13^*$	$61 \pm 26$
Max	104	70	99
Min	33	25	17
$n$	18	10	7

This summarizes the biophysical measurements we obtained from cells when grouped into fast, medium, and slow, as described in Figure 11; the input resistance ( $R_n$ ), including the maximum and minimum values, the time constant  $\tau_0$  values in ms and the number of cells ( $n$ ) in each group. Note that the slow group showed an average higher input resistance than the medium group; for this reason, it is unlikely that input resistance alone is the cause of the differential F/I properties among the groups. \*  $P < 0.025$ ; †  $P < 0.05$ . Values are means  $\pm$  SD.

### Physiological variability among retinal ganglion cells

Although good agreement between the physiological data and the model was revealed in this study, differences among the RGCs were noted in the slope of their impulse frequency versus current (F/I) responses. Figure 11 illustrates the results obtained from 35 cells that we classified into fast, medium, or slow groups based on their F/I response (cf. Caldwell and Daw 1978); 95% confidence limits are given for each group separately. As this figure illustrates, a significant difference was apparent between the fast and medium groups. All cells of these two groups exhibited stable repetitive firing for all levels of stimulus down to (at least) 10 pA. We defined, in addition, a slow group to include those cells that did not respond (or responded only sporadically) to 10 pA and whose spiking behavior was easily disrupted by virtually any fluctuation in membrane potential with 20 pA of stimulus.

Although the F/I response of most RGCs was inherently nonlinear, the average F/I slopes are  $\pm 1$  and 0.6 Hz/pA for

### Models of Leakage Contribution

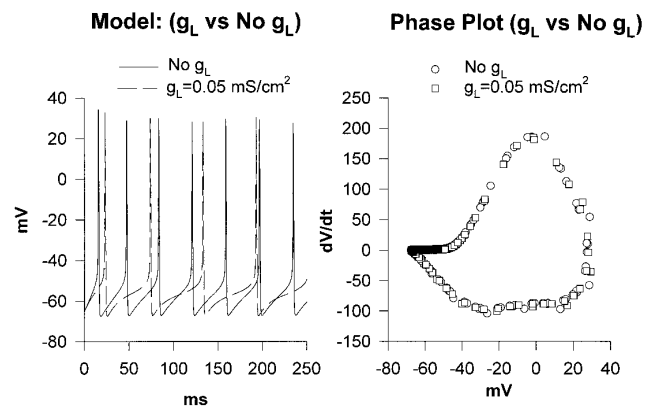


FIG. 10. A single-compartment model was studied in the absence of a leakage conductance (—) and the inclusion of a leakage conductance of  $0.05 \text{ mS/cm}^2$  (- - -). Presence of a leakage conductance reduced the rate of impulse activity in this case, although this effect depends on the value of  $V_L$ . Phase plot (right) illustrates that very little change in impulse waveform is introduced by the leakage.

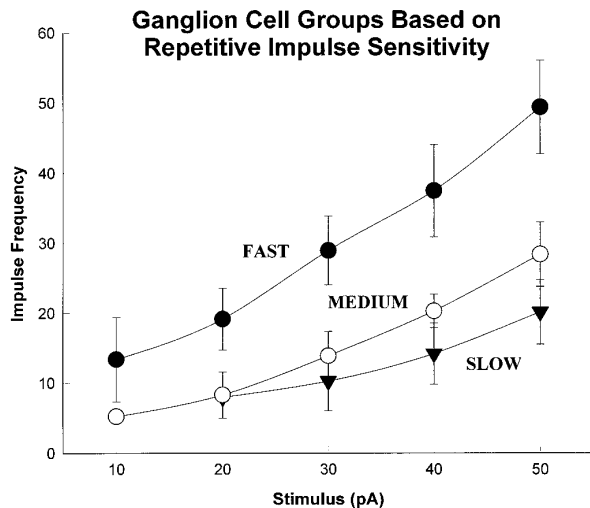


FIG. 11. Thirty-five cells were studied with different levels of current injection, and the results are plotted here as an F/I plot. We could distinguish 3 types of ganglion cells based on the F/I properties, which are shown with their 95% confidence limits. The fast cells had an F/I relationship of  $\sim 1$  Hz/pA, whereas the medium and slow cells were less activated. Slow group overlapped in their properties with the medium group but were distinguished by the ease with which the impulse train was interrupted by small perturbations in stimulus. It is important to recognize that this grouping of the cells does not relate in any way to the physiological type of cell, as ON, OFF, or ON-OFF, nor on the phasic vs. tonic properties of their light-evoked response. Virtually all retinal ganglion cells fired tonically when stimulus current was applied at the soma.

the fast and medium groups, respectively. Table 2 summarizes the biophysical measurements obtained from the three groups. While cells of the fast group did in general show the highest input resistance ( $1.45 \text{ G}\Omega$ ) and the longest time constant ( $65 \text{ ms}$ ), the slow group yielded a higher resistance on average than the medium group, yet with overall lower impulse frequencies. In view of the morphological heterogeneity displayed by RGCs (Arkin and Miller 1988; Toris et al. 1995), there was no reason to presuppose uniformity in their spike entrainment properties. Nevertheless, all RGCs ( $n = 35$ ) responded with tonic repetitive firing to depolarizing stimulus current in the soma, irrespective of their class of light evoked spiking pattern (ON, OFF, ON-OFF, transient or sustained); even transient ON-OFF RGCs, whose synaptic response amounted to no more than a few spikes, gave tonic responses to soma stimulation similar to those of cells that were activated tonically by illumination of the eyecup. Lipton and Tauck (1987) reached a similar conclusion in their study of rat retinal ganglion cells. In contrast, transient ON-OFF amacrine cells were encountered that did not respond with tonic repetitive firing to injected current, and this is consistent with an earlier study (Eliasof et al. 1987).

We find that the distinction in the F/I slope between fast and medium RGCs can be reproduced—in a single-compartment model—by changing the cell diameter from  $25 \mu\text{m}$  (fast) to  $35 \mu\text{m}$  (medium). This occurs because a given stimulus current (in picoamps) supplies charge to a larger total membrane capacitance in the larger diameter cell, resulting in a lower depolarization rate and prolonged interspike intervals. Thus the difference in single-compartment cell size may reflect differences in soma diameter and/or the amount of dendritic arbor present in fast, medium, and slow RGCs (cf. Fohlmeister and Miller 1997).

## DISCUSSION

When intracellular recordings are obtained from retinal ganglion cells with fine micropipettes, the impulses are often small and difficult to analyze. This is largely due to the high impedance of fine microelectrodes the time constants of which do not permit resolution of the impulse waveform with reliable fidelity. An additional factor may be that intracellular electrodes cause more shunting across the membrane and thus reduce the voltage excursions obtainable with small currents (Coleman and Miller 1989; Lipton and Tauck 1987). The introduction of patch electrode technology (Hamil et al. 1981) provided a means of obtaining stable recordings with low-resistance electrodes suitable for analysis of the impulse waveform. This method initially was applied exclusively to dissociated cells and subsequently was transferred to slice preparations, and our laboratory then succeeded in obtaining whole cell recordings from intact retinal ganglion cells (Coleman and Miller 1988). This technology thus has provided the means for the more quantitative analysis presented here.

Hodgkin and Huxley (1952) provided an elegant and biophysically detailed model for the nerve impulse, and we have maintained their basic model structure as well as their structure for the rate constants of voltage gating. Although the Hodgkin-Huxley model does fire repetitively when adequately stimulated, it has not been appropriate for modeling the repetitive firing in central neurons because of its rigid F/I properties and inability to generate low-impulse frequencies (Cooley and Dodge 1966; Guttman and Barnhill 1970). Improvements in this direction were advanced by Connor and Stevens (1971) who found and proposed that the  $I_{K,A}$  had appropriate kinetics to regulate the impulse firing rate in *Anisodora*. However, voltage-clamp analysis in rat (Lipton and Tauck 1987), tiger salamander (Lukasiewicz and Werblin 1988), and turtle (Lasater and Witkovsky 1991) has revealed that the kinetics of  $I_{K,A}$  are too fast to regulate the interspike interval significantly and that  $I_{K,A}$  was more likely to play a role in modulating impulse waveform. Our study supports this conclusion; thus  $I_{K,A}$  appears to play its most significant role during the repolarization phase of the impulse. The subsequent discovery of  $I_{K,Ca}$  (Latorre et al. 1989; Meech 1978) provided an additional mechanism by which impulse activity can be controlled through feedback from the impulses themselves; the occurrence of an impulse increases intracellular calcium, which activates  $g_{K,Ca}$  to prolong the subsequent interspike interval. The participation of calcium and calcium-activated potassium conductances previously has been invoked to account for intermittent bursting behavior in *Aplysia* (Adams et al. 1980; Gorman and Thomas 1978) and vertebrate neurons (Yarom et al. 1985) and thus  $I_{K,Ca}$  has become accepted as a mechanism for the control of the interspike interval (Hille 1992).

The findings of the present study for a typical (called fast) ganglion cell of the tiger salamander retina can be summarized as follows: constant current stimulation leads to tonic spike trains with an F/I relationship of  $\sim 1$  Hz/pA. Typical action potentials have amplitudes ranging from 70 to 90 mV, overshoot ground to about  $+20$  mV, have a width of  $\sim 1$  ms at half-amplitude and an upstroke velocity near  $200 \text{ V/s}$  ( $22^\circ\text{C}$ ). These impulse attributes were determined

with 400-ms duration current pulses under conditions in which light-evoked synaptic stimulation also could generate spiking. The cells exhibited input resistances of  $\sim 1\text{ G}\Omega$ , an average  $R_m$  of  $60\text{ k}\Omega \cdot \text{cm}^2$ , and resting potentials clustered about  $-65\text{ mV}$  in the dark. Both the physiological and computer simulation studies support the idea that  $I_{K,Ca}$  plays an important role in stabilizing the cell (i.e., in preventing spontaneous activity). Among the complement of ion channels investigated,  $I_{K,Ca}$  is unique in that it plays almost no role in the shaping of the impulse waveform per se, but is the dominant current during the interspike interval, where it contributes substantially to shaping the frequency of repetitive firing. However, it should be emphasized that impulse frequency is controlled by the currents of all channels acting in concert and in the presence of capacitative current. The single-compartment approximation is inherently incapable of exploring the equally important contribution to impulse frequency control of charge distributed electrotonically on neural processes (dendrites and axon) during interspike intervals, which forms the subject of the companion paper.

Although voltage-clamp data are critical for the identification of ion channels and their gating kinetics, the analysis of the voltage trajectory of an impulse train under current-clamp conditions is powerful and quite straightforward. Care must be taken, however, in determining the time derivative of the voltage trajectory. One approach used with large neurons such as cortical Betz cells, is the application of an analogue differentiating circuit. Betz cells generate substantially larger currents than retinal ganglion cells; they also generate action potentials with a rate-of-rise near  $600\text{ V/s}$  (Stafstrom et al. 1984a,b). Because of the slower rate-of-rise of action potentials generated by tiger salamander retinal ganglion cells (TS RGCs;  $200\text{ V/s}$ ), we were able to reliably determine  $dV/dt$  directly from our digitized data by use of the formulae given by Eqs. 1 and 2. The validity of these formulae, however, is limited to sufficiently high sampling rates whose lower bound depends on the value of the maximum  $dV/dt$  encountered. Our sampling rate of 5,000 points/s lies near that lower bound (see METHODS).

Although retinal ganglion cells may be relatively homogeneous with respect to their complement of ion channels, we did encounter significant differences among ganglion cells with regard to their F/I characteristics (Fig. 11). One possible explanation for these differences may lie in the properties of the ion channels themselves. Thus in the cat retina, Kaneda and Kaneko (1991b) demonstrated that inactivation of the Na current was more prolonged in W cells, which were identified retrogradely by DiI injections into the superior colliculus as opposed to the lateral geniculate. This could account for the "sluggish" firing of W cells. A similar phenomenon could possibly account for the slow cells observed in the present study. However, we note in the companion paper (Fohlmeister and Miller 1997) that cell morphology, including the structure of the dendritic tree, makes a substantial contribution to the control of the F/I relationship. In addition, other properties of the nerve impulse train, such as the long trajectory before the first impulse of the train, clearly are determined by cell morphology and could not be the result of modified Na inactivation. Thus although the composition and density of ion channels plays an important role in determining F/I relationships, cell morphology, con-

sidered in the following paper, cannot be dismissed in its importance and, in some cases, may play a significant role in the grouping of cells on the basis of impulse frequency generation.

We thank P. Coleman for providing experimental data and numerous stimulating discussions.

Address for reprint requests: J. F. Fohlmeister, Physiology Dept., 6-255 Millard Hall, University of Minnesota, 435 Delaware St. SE, Minneapolis, MN 55455.

Received 1 April 1996; accepted in final form 13 June 1997.

## REFERENCES

- ADAMS, P. R., SMITH, S. J., AND THOMPSON, S. H. Ionic currents in molluscan soma. *Annu. Rev. Neurosci.* 3: 141-167, 1980.
- ARKIN, M. S. AND MILLER, R. F. Mudpuppy retinal ganglion cell morphology revealed by an HRP impregnation technique which provides golgi-like staining. *J. Comp. Neurol.* 270: 185-208, 1988.
- BAYLOR, D. A. AND FETTIPLACE, R. Synaptic drive and impulse generation in ganglion cells of turtle retina. *J. Physiol. (Lond.)* 288: 107-127, 1979.
- BELGUM, J. H., DVORAK, D. R., AND MCREYNOLDS, J. S. Sustained and transient synaptic inputs to on-off ganglion cells in the mudpuppy retina. *J. Physiol. (Lond.)* 340: 599-610, 1983.
- BEZANILLA, F. AND ARMSTRONG, C. M. Inactivation of the sodium channel. I. Sodium current experiments. *J. Gen. Physiol.* 70: 549-566, 1977.
- CALDWELL, J. H. AND DAW, N. W. New properties of rabbit retinal ganglion cells. *J. Physiol. (Lond.)* 276: 257-276, 1978.
- CARRAS, P. L., COLEMAN, P. A., AND MILLER, R. F. Site of action potential initiation in amphibian retinal ganglion cells. *J. Neurophysiol.* 67: 292-304, 1992.
- CHAD, J., KALMAN, D., AND ARMSTRONG, D. The role of cyclic AMP-dependent phosphorylation in the maintenance and modulation of voltage-activated calcium channels. In: *Cell Calcium and the Control of Membrane Transport*, edited by L. J. Mandel and D. C. Eaton. New York: Rockefeller Press, 1987, p. 167-186.
- COLE, K. S. *Membranes, Ions and Impulses*. Berkeley: Univ. of California Press, 1968.
- COLE, K. S. AND MOORE, J. W. Potassium ion current in the squid giant axon: dynamic characteristic. *Biophys. J.* 1: 1-14, 1960.
- COLEMAN, P. A. AND MILLER, R. F. Measurement of passive membrane parameters with whole-cell recording from neurons in the intact amphibian retina. *J. Neurophysiol.* 61: 218-230, 1989.
- CONNOR, J. A. AND STEVENS, C. F. Voltage clamp studies of a transient outward membrane current in gastropod neural somata. *J. Physiol. (Lond.)* 213: 21-30, 1971.
- COOLEY, J. W. AND DODGE, F. A., JR. Digital computer solutions for excitation and propagation of the nerve impulse. *Biophys. J.* 6: 583-599, 1966.
- COOMBS, J. S., CURTIS, D. R., AND ECCLES, J. C. The interpretation of spike potentials of motoneurons. *J. Physiol. (Lond.)* 139: 198-231, 1957.
- ELIASOF, S., BARNES, S., AND WERBLIN, F. The interaction of ionic currents mediating single spike activity in retinal amacrine cells of the tiger salamander. *J. Neurosci.* 7: 3512-3524, 1987.
- FOHLMEISTER, J. F., COLEMAN, P. A., AND MILLER, R. F. Modeling the repetitive firing of retinal ganglion cells. *Brain Res.* 510: 343-345, 1990.
- FOHLMEISTER, J. F., AND MILLER, R. F. Mechanisms by which cell geometry controls repetitive impulse firing in retinal ganglion cells. *J. Neurophysiol.* 78: 1948-1964, 1997.
- FOHLMEISTER, J. F., POPPEL, R. E., AND PURPLE, R. L. Repetitive firing: quantitative analysis of encoder behavior of slowly adapting stretch receptor of crayfish and eccentric cell of *Limulus*. *J. Gen. Physiol.* 69: 849-877, 1977.
- FRUMKES, T. E., MILLER, R. F., SLAUGHTER, M., AND DACHEUX, R. F. Physiological and pharmacological basis of GABA and glycine action on neurons of mudpuppy retina. III. Amacrine-mediated inhibitory influences on ganglion cell receptive-field organization: a model. *J. Neurophysiol.* 45: 783-804, 1981.
- GORMAN, A. L. AND THOMAS, M. V. Changes in the intracellular concentration of free calcium ions in a pace-maker neurone, measured with the metallochromic indicator dye arsenazo III. *J. Physiol. (Lond.)* 275: 357-376, 1978.
- GUTTMAN, R. AND BARNHILL, R. Oscillation and repetitive firing in squid

- axons. Comparison of experiments with computations. *J. Gen. Physiol.* 55: 104–118, 1970.
- HAMIL, O. P., MARTY, A., NEHER, E., AND SIGWORTH, F. J. Improved patch-clamp techniques for high resolution current recording from cells and cell-free membrane patches. *Pflügers Arch.* 391: 473–496, 1981.
- HILLE, B. Potassium channels and chloride channels. In: *Ionic Channels of Excitable Membranes*. Sunderland, MA: Sinauer Associates, 1992, p. 115–139.
- HODGKIN, A. L. AND HUXLEY, A. F. A quantitative description of membrane current and its applications to conduction and excitation in nerve. *J. Physiol. (Lond.)* 117: 500–544, 1952.
- HUGUES, M., ROMEY, G., DUVAL, D., VINCENT, P., AND LAZDUNSKI, M. Apamin as a selective blocker of the calcium dependent potassium channel in neuroblastoma cells: voltage-clamp and biochemical characterization of the toxin receptor. *Proc. Natl. Acad. Sci. USA* 79: 1308–1312, 1982.
- KANEDA, M. AND KANEKO, A. Voltage-gated calcium currents in isolated retinal ganglion cells of the cat. *Jpn. J. Physiol.* 41: 35–48, 1991a.
- KANEDA, M. AND KANEKO, A. Voltage-gated sodium currents in isolated retinal ganglion cells of the cat: relation between the inactivation kinetics and the cell type. *Neurosci. Res.* 11: 261–275, 1991b.
- KARSCHIN, A. AND LIPTON, S. A. Calcium channels in solitary retinal ganglion cells from post-natal rat. *J. Physiol. (Lond.)* 418: 379–396, 1989.
- LASATER, E. M. AND WITROVSKY, P. Membrane currents of spiking cells isolated from turtle retina. *J. Comp. Physiol. [A]* 167: 11–21, 1990.
- LATORRE, R., OBERHAUSER, A., LABARCA, P., AND ALVAREZ, O. Varieties of calcium-activated potassium channels. *Annu. Rev. Physiol.* 51: 385–399, 1989.
- LIPTON, S. A. AND TAUCK, D. L. Voltage-dependent conductances of solitary ganglion cells dissociated from the rat retina. *J. Physiol. (Lond.)* 385: 361–391, 1987.
- LUKASIEWICZ, P. AND WERBLIN, F. A slowly inactivating potassium current truncates spike activity in ganglion cell of the tiger salamander retina. *J. Neurosci.* 8: 4470–4481, 1988.
- MEECH, R. W. Calcium-dependent potassium activation in nervous tissues. *Annu. Rev. Biophys. Bioeng.* 7: 1–18, 1978.
- ROGAWSKI, M. A. Aminopyridines enhance opening of calcium-activated potassium channels in GH3 anterior pituitary cells. *Mol. Pharmacol.* 35: 458–468, 1989.
- STAFSTROM, C. E., SCHWINDT, P. C., AND CRILL, W. E. Properties of subthreshold response and action potential recorded in layer V neurons from cat sensorimotor cortex in vitro. *J. Neurophysiol.* 52: 244–263, 1984a.
- STAFSTROM, C. E., SCHWINDT, P. C., FLATMAN, J. A., AND CRILL, W. E. Repetitive firing in layer V neurons from cat neocortex in vitro. *J. Neurophysiol.* 52: 244–263, 1984b.
- TORIS, C. B., EIESLAND, J. L., AND MILLER, R. F. Morphology of ganglion cells in the neotenus tiger salamander retina. *J. Comp. Neurol.* 352: 535–559, 1995.
- YAROM, Y., SUGIMORI, M., AND LLINAS, R. Ionic currents and firing patterns of mammalian vagal motoneurons. *J. Neurosci.* 16: 719–737, 1985.